◆ Human Brain Mapping 35:5219–5235 (2014) ◆

The Dual Facet of Gamma Oscillations: Separate Visual and Decision Making Circuits as Revealed by Simultaneous EEG/fMRI

João Castelhano,[1,2] Isabel Catarina Duarte,[2] Michael Wibral,[3] Eugénio Rodriguez,[4] and Miguel Castelo-Branco[1,2]*

[1]*Visual Neuroscience Laboratory, IBILI—Institute for Biomedical Imaging and Life Sciences, Faculty of Medicine, University of Coimbra, Coimbra, Portugal*
[2]*ICNAS—Institute for Nuclear Sciences Applied to Health, University of Coimbra, Coimbra, Portugal*
[3]*Brain Imaging Center, J.W. Goethe University, Frankfurt am Main, Germany*
[4]*Escuela de psicologia, Pontificia Universidad Católica de Chile, Santiago, Chile*

Abstract: It remains an outstanding question whether gamma-band oscillations reflect unitary cognitive processes within the same task. EEG/MEG studies do lack the resolution or coverage to address the highly debated question whether single gamma activity patterns are linked with multiple cognitive modules or alternatively each pattern associates with a specific cognitive module, within the same coherent perceptual task. One way to disentangle these issues would be to provide direct identification of their sources, by combining different techniques. Here, we directly examined these questions by performing simultaneous EEG/fMRI using an ambiguous perception paradigm requiring holistic integration. We found that distinct gamma frequency sub-bands reflect different neural substrates and cognitive mechanisms when comparing object perception states *vs*. no categorical perception. A low gamma sub-band (near 40 Hz) activity was tightly related to the decision making network, and in particular the anterior insula. A high gamma sub-band (∼60 Hz) could be linked to early visual processing regions. The demonstration of a clear functional topography for distinct gamma sub-bands within the same task shows that distinct gamma-band modulations underlie sensory processing and perceptual decision mechanisms. *Hum Brain Mapp 35:5219–5235, 2014.*

Key words: gamma-band oscillations; simultaneous EEG/fMRI; source localization; visual perception; cognitive modules; multimodal imaging

Additional Supporting Information may be found in the online version of this article.

*Correspondence to: Miguel Castelo-Branco, Visual Neuroscience Laboratory, IBILI-Faculty of Medicine, University of Coimbra, Azinhaga de Santa Comba, 3000-548 Coimbra, Portugal.
E-mail: mcbranco@fmed.uc.pt

Contract grant sponsor: BIN (the Brain Imaging Network of Portugal); Contract grant number: FP7-HEALTH-2013-INNOVATION—1—602186—BRAINTRAIN; Contract grant sponsor: Compete PEST; Contract grant numbers: C/SAU/UI3282/2014-COMPETE, PTDC/SAU-ORG/118380/2010; Contract grant sponsor: Bial Foundation Projects 132 and 133/12; Contract grant number: CENTRO-07-ST24-FEDER-00205; Contract grant sponsor: FCT Portugal; Contract grant number: SFRH/BD/65341/2009.

Received for publication 16 February 2014; Revised 1 May 2014; Accepted 2 May 2014.

DOI: 10.1002/hbm.22545
Published online 16 May 2014 in Wiley Online Library (wileyonlinelibrary.com).

INTRODUCTION

It has been proposed that gamma-band activity signals emerging object percepts and decision-making [Gruber et al., 2001; Martinovic et al., 2008; Rodriguez et al., 1999; Sedley and Cunningham, 2013]. Accordingly, gamma-band modulation is increased for ambiguous states prior to a perceptual decision [Castelhano et al., 2013]. Animal studies [Castelo-Branco et al., 1998; Varela et al., 2001] further support the ability to form coherent Gestalts [Keil et al., 1999] as a function of gamma, in addition to the earlier mentioned signaling of emerging object percepts.

Furthermore, gamma oscillations have been related to many cognitive processes [Crone et al., 2011; Fries, 2009; Gruber et al., 2001; Jensen et al., 2007; Rodriguez et al., 1999; Tallon-Baudry and Bertrand, 1999]. Hence, electrophysiological studies showed a wide variety of gamma-band patterns and sources for different tasks [Akimoto et al., 2013; Edwards et al., 2005; Fries et al., 2008; Gruber et al., 2008; Grützner et al., 2010; Jerbi et al., 2009; Lachaux et al., 2005; Ray and Maunsell, 2011; Uchida et al., 2001] but not within the same type of cognitive task. Accordingly, it remains unclear whether distinct patterns related to different cognitive modules coexist in the same task. Unimodal studies do not have enough resolution to test for nonunitary sources and to establish their spatial distribution [Crone et al., 2011; Uhlhaas et al., 2011]. It is known that gamma patterns occur in a distributed manner across cortical regions [Groppe et al., 2013; Guggisberg et al., 2007; Lachaux et al., 2005] and even at different frequency ranges [Crone et al., 2011; Hoogenboom et al., 2006; Sedley and Cunningham, 2013; Uhlhaas et al., 2011]. A major question is however still open: is there a single gamma activity pattern of a broad frequency band that reflects perception [Gruber et al., 2001; Rodriguez et al., 1999], decision mechanisms [Guggisberg et al., 2007] or both or, on the other hand, are there separable gamma narrow sub-bands with distinct spatial sources in the brain?

In line with this notion, earlier experiments (in particular in animals) suggested that low- and high-frequency oscillatory sub-bands may indeed reflect different neural processes and may be originated in distinct brain regions [Guggisberg et al., 2007; Ray and Maunsell, 2011; Scheeringa et al., 2011]. In this line, a recent MEG study also showed a dissociation of attentional processes influencing higher gamma oscillations in early visual cortex, but not higher visual cortex, with clear distinct source localization for distinct frequency sub-bands, but within the same region (lateral and medial visual cortex [Koelewijn et al., 2013]. Interestingly, we have also identified two distinct patterns of gamma-band activity for the moment a holistic object percept is formed [Bernardino et al., 2013; Castelhano et al., 2013]. These were observed in a perceptual decision paradigm requiring object recognition from 3D structure-from-motion in normal subjects and in a clinical model of impaired perceptual coherence [Bernardino et al., 2013]. A low range gamma sub-band (near 40 Hz) was increased in patients while a higher gamma narrow band (~60 Hz) was increased in controls, suggesting the use of distinct cognitive modules. This finding inspired us to test whether a critical dissociation exists between low and high gamma-band oscillations [Sedley and Cunningham, 2013]. If they reflect nonunitary processes, that would be relevant to understand normal cognition and neuropsychiatric disorders such as autistic spectrum disorder and schizophrenia [Bernardino et al., 2013; Uhlhaas and Singer, 2012], which are clinical models of fragmented perception and decision.

Despite the technical challenges, simultaneous recordings of electrophysiological and hemodynamic activity can be successfully measured [Allen et al., 1998; Brookes et al., 2009; Duarte et al., 2013; Freyer et al., 2009; Mandelkow et al., 2006; Ritter and Villringer, 2006; Rosenkranz and Lemieux, 2010] and potentially clarify the contribution and sources of relatively narrow low- and high- frequency neuronal dynamics [Guggisberg et al., 2007; Ray and Maunsell, 2011; Scheeringa et al., 2011] given their complementary advantages [Foucher et al., 2003; Freyer et al., 2009] and coverage [Herrmann and Debener, 2008; Laufs, 2008; Ritter and Villringer, 2006]. Besides, despite the known limitation of EEG/fMRI, gamma-band activity can be assessed using this technique at least in the 25–75 Hz range [Brookes et al., 2009; Mandelkow et al., 2006; Mantini et al., 2007b] and linked to the Blood oxygen level dependent (BOLD) fMRI response [Lachaux et al., 2007; Logothetis, 2008; Logothetis et al., 2001; Niessing et al., 2005], as assessed by general linear models [Michels et al., 2010; Sumiyoshi et al., 2012] in humans performing a cognitive task [Scheeringa et al., 2011].

To investigate the neuronal sources of gamma-band responses to ambiguous perceptual states [Lachaux et al., 2005; Laufs, 2008] with high spatial resolution, we performed simultaneous EEG/fMRI recordings. Our hypothesis was that independent gamma processes underlie visual perception and decision. We used a face/object detection and categorization task that was previously shown to increase gamma-band activity patterns [Castelhano et al., 2013; Rebola et al., 2012; Rodriguez et al., 1999]. Increased activity was found to perception *vs.* no-perception states. We predicted that separable sources of gamma-band activity should be identified in relation to different cognitive processes by means of an EEG-informed fMRI approach. This strategy implements EEG pre-processing to obtain a specific EEG feature (time-frequency activity within a specific frequency band [Scheeringa et al., 2009]) that can be used as predictor for the general linear model (GLM) analysis of simultaneous fMRI data [Debener et al., 2006]. We found that low gamma (30–48 Hz) response is related to general perceptual decision-making networks and high gamma activity (52–70 Hz) is associated with low level visual processing. These nonunitary patterns are relevant for the understanding of normal and clinical impaired holistic

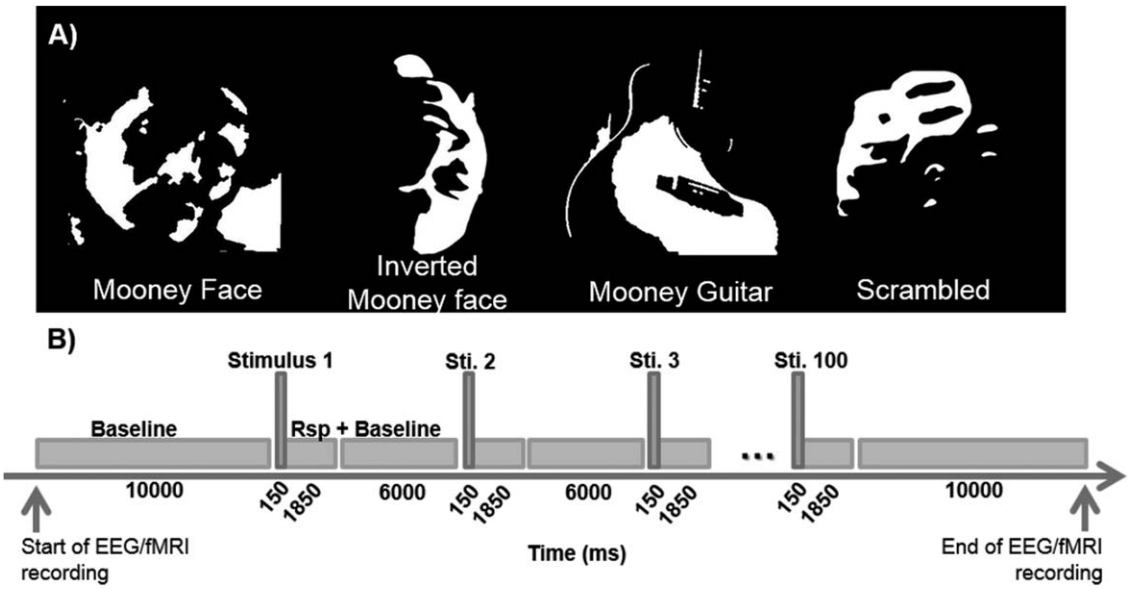

Figure 1.

Task timeline. (**A**) Examples of Mooney object categories and scrambled controls. (**B**) Timeline details; Each run started with a black screen for 10,000 ms and contained 100 trials (25 trials of each category). Three runs were performed during the experiment (one outside scanner and two inside scanner). Stimuli were presented for 150 ms in a trial that lasted for 2,000 ms. The average inter-stimulus-interval (fixation cross on a black screen) was 7,850 ms (slow event-related design). Stimulus presentation was randomized across subjects and runs, and there were no repetitions. Subjects had to discriminate between categories (face, guitar, or other) and to press the respective button in the response box only after stimulus disappearance. EEG and fMRI recordings were done concurrent with stimulus presentation.

integration and show that current neural models of gamma activity generation need to consider their duality.

MATERIALS AND METHODS

Subjects

We performed a simultaneous EEG/fMRI experiment in ten healthy subjects (age = 26.33 ± 4.17 years; six males; two left handed). All participants had normal or corrected-to normal vision and no history of neurological disorders and were naive regarding the purpose of the study. All subjects performed the simultaneous EEG/fMRI task (two runs) and one prior run of EEG recording outside the scanner. This study was approved by the Ethics Commission of the Faculty of Medicine of the University of Coimbra and was conducted in accordance with the declaration of Helsinki. All subjects gave written informed consent to participate in the study.

Stimuli

Visual stimuli were Mooney pictures (black and white incomplete stimuli [Mooney, 1957]) of faces (upright and inverted), guitars (prototypical stimuli), and their scrambled versions (see Fig. 1 for examples). Stimuli were presented using Presentation software (Neurobehavioral Systems). Subjects viewed the projected (LCD Projector, Avotec, USA) stimuli in a white screen located at the back of the scanner (stimulus size: $6.56° \times 6.60°$) through a mirror placed on the head coil.

Procedure

The experiment consisted of three runs of EEG recordings: two runs were collected during fMRI acquisition and one outside the scanner. fMRI was acquired concurrently with the EEG recordings. Each run included 25 Mooney face stimuli, 25 inverted Mooney faces, 25 Mooney guitars, and 25 scrambled Mooney events. In total we had 50 trials of each condition for the recordings obtained inside the scanner. The number of trials for perceived faces *vs*. non faces stimuli was approximately identical thus precluding possible response-related attentional effects. Recognition of Mooney objects was previously linked to increased gamma-band activity [Castelhano et al., 2013; Rebola et al., 2012; Rodriguez et al., 1999]. Stimulus presentation was randomized across runs and subjects, and no stimulus was repeated to prevent repetition induced effects. The trial duration was 2 s, during which one stimulus was presented for 150 ms. Stimulus presentation was triggered

automatically by the fMRI pulse. The stimuli (see Fig. 1) were randomly presented with an average inter-stimulus interval of 7,850 ms. A fixation cross on a dark screen was shown during the baseline periods. Subjects performed a forced choice discrimination task between the Mooney categories and were asked to press one of three keys after the image presentation to discriminate between faces, guitars, and scrambled stimuli. Note that responses were required only after the stimulus offset (for details on reaction times see results section), to prevent early contamination from motor responses.

EEG Recording

For EEG recording we used an MR compatible EEG system (MagLink™, NeuroScan, USA) with a cap providing 64Ag/AgCl nonmagnetic electrodes positioned according to the extended 10/20 system. The recording reference was set to an electrode close to CZ and EEG and fMRI data were acquired in a continuous way. The EEG signal was amplified and recorded at a sampling rate (SR) of 10 kHz. This high SR is necessary to sample accurately the gradient artifact. The amplifier was located and connected to a PC in the scanner control room. To improve the effectiveness of the offline artifact correction algorithms, EEG and fMRI recordings were synchronized by means of a Syncbox (NordicNeuroLab, USA) [Ertl et al., 2010; Mandelkow et al., 2006]. The exact timing of stimulus onset and MRI scanner gradient switching were recorded together with the EEG signal as well as with the stimuli logfiles. VEO and HEO bipolar channels were used to record EOG and two more channels were placed in the standard EKG electrode positions for EKG recordings. These data were required to detect the ballistocardiogram (BCG) artifacts in the EEG recordings. All artifacts (gradient artifact and BCG) were removed offline (see below). Channels that did not fulfill the impedance criteria ($<15\Omega$) or had problems during acquisition were marked as "bad" and excluded (>55 channels per subject were available for final analysis). To overcome this issue for group average results, the spherical interpolation of missing channels for each subject was used as it is implemented in EEGLAB (Matlab® toolbox v10_2_5_6a; [Delorme and Makeig, 2004]).

Functional MRI Recording

MR imaging data were acquired on a 3T whole-body MR scanner (Siemens Trio) using a 12 channel head coil. Anatomical images were collected using a T_1 weighted MPRAGE (magnetization-prepared rapid-acquisition gradient echo). T_2*-weighted gradient-echo echo planar imaging was used to collect fMRI data with TR = 2 s, TE = 39 ms, 27 slices per TR, 2.5 × 2.5 in-plane resolution, 3.5 mm slice thickness with 4.2-mm gap, flip angle = 90° and matrix size = 102 × 102. The slices were oriented to obtain whole brain coverage. Nearly 410 volumes were acquired for each run with a total scan time of 13:40 min. All runs were acquired in the same EEG/fMRI session. The first three volumes were discarded from the analysis. Data analysis was performed using BrainVoyager QX v2.4 (Brain Innovation, Maastricht, The Netherlands).

EEG Data Analysis

Analysis of EEG data acquired concurrently with fMRI

Concurrent EEG/fMRI is challenging due to gradient artifacts (which are related to gradient switching) and ballistocardiogram signals (BCG; which represent physiological cardiac-related artifacts) [Allen et al., 2000]. Several methods have been developed for offline correction of the data [Allen et al., 1998, 2000; De Munck et al., 2013; Debener et al., 2008; Gonçalves et al., 2007]. EEG artifacts related to MR gradient switch were corrected offline using average subtraction gradient correction implemented in Maglink RT Edit software (v4.5, NeuroScan, USA). In brief, this creates an average template of the artifact that is subtracted from the recorded EEG [Allen et al., 1998, 2000]. The correction algorithm includes a low-pass filter of 75 Hz.

BCG artifacts were corrected using independent component analysis (ICA) [Mantini et al., 2007a] implemented in EEGLAB (Matlab® toolbox v10_2_5_6a; [Delorme and Makeig, 2004]). The independent components were inspected and the ones with higher correlation with the EKG signal recorded during the acquisition were removed from the signal. ICA, based on all electrodes (including 4 EOG channels), was also applied to perform correction of eye movement related artifacts as performed in Keren et al., [2010]. We used the scalp topography of the ICA components to identify the ocular component for ocular artifact attenuation. All channels were re-referenced to average reference. Epochs (−500 ms to 1,000 ms) were obtained locked to the beginning of the correctly reported stimuli and automatic epoch rejection as implemented in the EEGLAB toolbox was then applied with an amplitude criteria of ±75 μV followed by visual inspection. After epoch rejection 84.5% ± 7.23% (mean ± standard deviation) epochs of faces, 83.75% ± 12.07% epochs of inverted faces, 82.5% ± 8.26% epochs of guitars, and 83.75% ± 13.48% epochs of the scrambled condition per subject remained for further analysis.

Time–frequency analysis was implemented as in Uhlhaas et al., [2006] and is described elsewhere [Bernardino et al., 2013; Castelhano et al., 2013; Lachaux et al., 1999; Rodriguez et al., 1999]. This analysis was carried out in Matlab® concerning induced (non-phase locked) activity for frequencies ranging from 10 to 70 Hz (feasible range within the limitations of EEG/fMRI) in steps of 1 Hz for all channels. Time-frequency data were normalized (in the z-score sense) to the baseline defined to pre-stimulus time-window (−500 ms to −50 ms) by subtracting the mean of the baseline per frequency bin and dividing by their standard deviation.

Results are shown for a cluster of parieto-occipital and temporal electrodes (PO7, PO5, PO3, POZ, PO4, PO6, PO8, CP5, TP7, P5, P7, CP6, TP8, P6, and P8) [Bernardino et al., 2013].

For the statistical comparison between conditions, for each time-frequency point, nonparametric statistics (Mann–Whitney *U* tests, Wilcoxon rank sum test) were carried out and Bonferroni–Holms correction for multiple comparisons (*P* values divided by the number of comparisons) were applied when appropriate. Furthermore, Pearson correlation was computed to assess if the reaction time covariate did explain the observed pattern of results.

Event-related potential (ERP) measures were also obtained. Data were filtered between 1 and 30 Hz and segmented into epochs (−100 to 500 ms) locked to stimulus onset. After baseline correction (prestimulus interval) ERPs were obtained averaging the remaining trials per condition. One-Way ANOVA with Bonferroni correction was computed to assess statistical significance of the resulting ERPs.

ERP analysis of EEG data acquired outside the scanner

EEG data recorded outside the scanner were processed offline using the Scan 4.5 Edit Software (NeuroScan, USA) and EEGLab (Matlab®). ICA-based ballistocardiogram correction was performed to ensure that processing was exactly identical to the one performed inside the scanner. Data were filtered between 1 and 30 Hz and segmented into epochs (−100 to 500 ms) locked to stimulus onset. After baseline correction based on the interval before stimulus onset the automatic epoch rejection (followed by visual inspection) was applied with a criteria set to ±75 μV (with >88% of the trials accepted for further processing). The epochs were organized by stimulus type and event related potentials (ERP) were obtained. One-way ANOVA statistical testing was performed to assess differences between conditions and Bonferroni correction was used to correct for multiple comparisons.

ERP Source Localization

We performed source localization of the EEG data as it is implemented in Curry 7.0 software (NeuroScan, USA) on a realistic head model. For each condition, group average ERP data were coregistered with anatomical MR data using landmarks and standard electrode positions. Standard anatomical MR data were used to create the boundary element model (BEM) and current source density (CSD) analysis was performed. CSD computes a local current pattern that explains the EEG data at a certain time-point. The CSD source localization was based in sLORETA (standardized low resolution brain electromagnetic tomography) method [Pascual-Marqui et al., 1994] with no assumption regarding the number or location of active sources. This method is a standardized discrete, three-dimensional (3D) distributed, linear weighted Minimum norm inverse solution that takes several neurophysiologic and anatomical constraints into account and has been shown to yield depth-compensated zero localization error inverse solutions [Pascual-Marqui, 1999; Pascual-Marqui et al., 2002]. sLORETA employs the current density estimate given by the minimum norm solution, and localization inference is based on standardized values of the current density estimates [Pascual-Marqui, 2002]. It was computed in Curry 7.0 yielding an estimate of activity measures [Pascual-Marqui, 2002], namely (for each location) the current strength divided by its error bar, from which a F-distribution of the current densities were extracted. This is not a statistical estimate in a strict sense and therefore it has only localizing value and not in the comparison of activities across sources, which justifies that some caution should be taken regarding interpretations of such activated sources. Source localization plots were computed for a 200 ms time-window including the N170 peak.

fMRI Data Analysis

Functional MRI data were analyzed (pre-processing and statistical analysis) using BrainVoyager QX 2.4 (Brain Innovation, Maastricht, The Netherlands). The first three volumes were discarded to avoid saturation effects. Preprocessing was performed with the default parameters including 3D motion correction, spatial smoothing and temporal high-pass filtering of 0.00980 Hz (three cycles in time course). The images were transformed into Talairach space. This is a limitation of the study since this atlas template is based in only one subject. fMRI data were coregistered with anatomical data and statistical fMRI analysis was performed using the general linear model (GLM), as implemented in BrainVoyager QX.

Gamma-Band Source Localization

First, to localize the sources of Gamma activity in two distinct frequency ranges, low (30–48 Hz; LF) and high frequency (52–70 Hz; HF) per stimulus condition we performed time-frequency decomposition using Curry 7.0 software. The 48–52 Hz range was excluded to avoid line noise. We performed this frequency analysis using the short time fast Fourier transform (STFFT) as implemented in Curry 7.0 software. It provides time and frequency representation of the signal with high temporal resolution for the faster frequencies. Source localization was performed for all accepted channels combined. The resulting source analysis time points for each condition are based on the latencies of the time-frequency peaks extracted from the group average data over all parieto-occipital and temporal electrodes (see above) and locked to the beginning of the stimulus. This was performed for the low and high frequency ranges (data filtered between 30 and 48 Hz and between 52 and 70 Hz, respectively). Using the same procedure as in the ERP source localization we calculated the current source density maps from the group data, as revealed by sLORETA for these gamma-frequency ranges.

Furthermore, to precisely localize the active regions we performed an EEG-informed fMRI approach in which an EEG time-frequency feature is extracted from EEG data

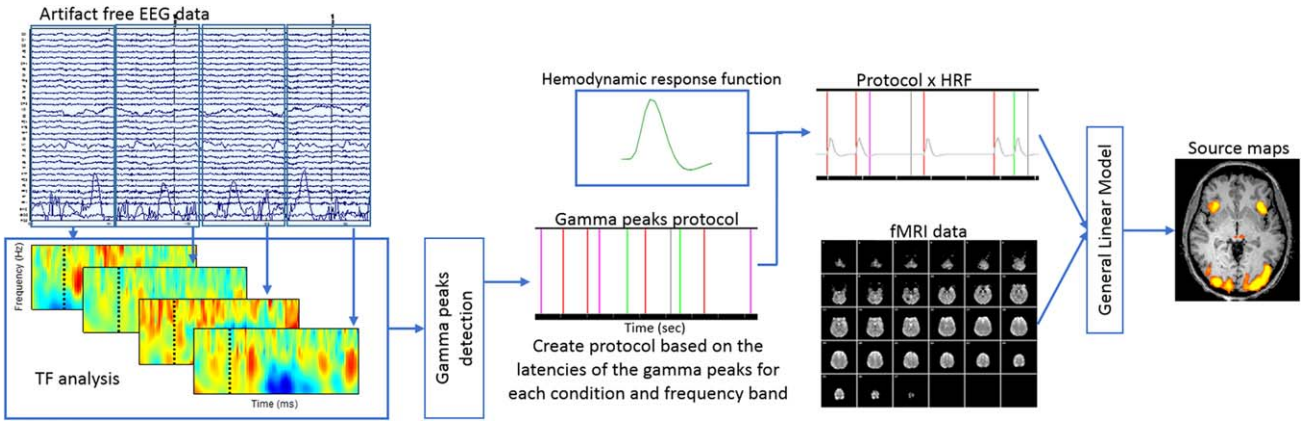

Figure 2.

Schematic representation of EEG-informed fMRI analysis. After artifact correction, EEG data (acquired concurrently with fMRI) were split into 2-s epochs and time-frequency (TF) decomposition applied. For each epoch that contains an event of interest (perceptual conditions) the latency of the maximum of gamma activity was extracted and used to build the fMRI protocol. Separated low and high gamma frequency events for each condition were used as predictors. After convolution with the hemodynamic response function (HRF), a general linear model (GLM) analysis was performed in fMRI data and the resulting statistical source maps show the sources of gamma activity peaks (see [Huster et al., 2012]). [Color figure can be viewed in the online issue, which is available at wileyonlinelibrary.com.]

and used to inform fMRI GLM analysis (Fig. 2 schematically shows how this approach is performed) [Debener et al., 2006; Huster et al., 2012; Nguyen and Cunnington, 2014; Scheeringa et al., 2009].

Consecutive time–frequency analysis epochs of 2 s were applied to detect oscillations induced but not necessarily phase locked neither to the stimuli nor to the response. Concerning EEG-informed fMRI, as we found similar time–frequency results and current density source patterns for all readily perceived object categories, we used all Mooney object (faces + guitars) stimuli together *vs.* scrambled + inverted faces (difficult perceptual decision conditions). This analysis using balanced number of trials focused more on the issue of difficult perceptual decision. Separate EEG regressors for each condition (object and scrambled) from low (30–48 Hz [Hoogenboom et al., 2006]) and high (52–70 Hz [Akimoto et al., 2013]) frequency bands were constructed. The peak latencies were obtained on a trial by trial basis per subject, in the two gamma sub-bands of interest and calculated by averaging time-frequency results over the same parieto-occipital and temporal electrodes as before. The resulting predictors were introduced in the general linear model (GLM) design matrix [Huster et al., 2012; Laufs, 2008; Michels et al., 2010] as in event-related fMRI designs. Contrasts were computed against the baseline (with epochs without any peak neither in LF nor HF sub-bands). Statistical maps show the results for LF and HF based contrasts for a whole-brain analysis when computing the above mentioned contrasts. Corrections for multiple comparisons were made through the Cluster Threshold plugin (BrainVoyager QX) with 1,000 iterations. The minimum cluster size was set to a significant voxel threshold of $P < 0.05$ for each contrast. *T*-tests were applied between conditions in each frequency band and the coordinates and statistical results of the peak analysis for all clusters (of increased or decreased BOLD signal) are summarized in Table I.

RESULTS

Behavioral Data

To study the neural underpinnings of EEG oscillations, we used a categorical perception task in which subjects had to discriminate between Mooney (two-tone incomplete patterns) object categories (Fig. 1). Behavioral analysis showed that participants were well above chance in terms of categorization performance levels (96.79% ± 3.13% for "guitar-like" stereotypical objects; 81.4% ± 13.3% and 81.06% ± 13.46% for upright and inverted mooney faces, respectively; 75.79% ± 18.90% for scrambled control stimuli; values indicate mean ± standard deviation, except when otherwise indicated). An ANOVA revealed a main effect for condition ($F = 18.156$, $P < 0.00001$) and the post-hoc Bonferroni tests showed that these differences in discrimination rates were significant between faces and guitars (Mean difference: 20.51, $P < 0.0001$), inverted faces and guitars (mean difference: 12.08, $P = 0.027$), guitars versus scrambled (mean difference: 29.00, $P < 0.0001$) and inverted faces vs. scrambled (mean difference: 16.93, $P = 0.001$). A bar graph summarizing these results is shown in Figure 3 (left panel). This shows that subjects were best at guitar discrimination. Regarding reaction

TABLE I. Location and statistics of significantly activated brain regions (clusters) for the different contrasts of GLM analysis (distinct conditions and frequency ranges)

		Peak *X*	Peak *Y*	Peak *Z*	*t*	*P*	#Voxels	Brain region
Faces and guitars LF	Cluster 1	56	−50	27	3,065	0.0022	1136	R, Parietal Lobe, Supramarginal Gyrus,BA40
	Cluster 2	35	22	0	3,651	0.0003	2427	R, Sub-lobar, Insula, BA13
	Cluster 3	2	22	39	3,119	0.0018	2647	R, Limbic Lobe, Cingulate Gyrus, BA32
	Cluster 4	−10	−71	12	3,307	0.0009	3850	L, Occipital Lobe, Cuneus, BA17
	Cluster 5	−37	−71	−15	4,061	0.00005	3207	L, Posterior Lobe, Declive
	Cluster 6	−22	−47	24	3,485	0.0005	936	L, Limbic Lobe, Cingulate Gyrus, BA31
Inv.Faces and scrambled LF	Cluster 1	−4	34	0	−3,325	0.0009	6054	L, Limbic Lobe, Anterior Cingulate
	Cluster 2	5	−35	66	−3,675	0.0002	1106	R, Frontal Lobe, Paracentral Lobule, BA4
	Cluster 3	−4	−93	30	−3,851	0.0001	2092	L, Occipital Lobe, Cuneus, BA19
	Cluster 4	−28	−38	21	−3,764	0.0002	2157	L, Sub-lobar, Insula, BA13
	Cluster 5	−19	−86	36	−3,018	0.0025	763	L, Occipital Lobe, Cuneus, BA19
	Cluster 6	−31	19	9	3,268	0.0011	737	L, Sub-lobar, Insula, BA13
	Cluster 7	−61	−32	0	−3,359	0.0008	942	L, Temporal Lobe, Middle Temporal Gyrus
Faces and guitars HF	Cluster 1	59	−14	18	−4,076	0.00005	4462	R, Parietal Lobe, Postcentral Gyrus, BA43
	Cluster 2	29	−44	60	−3,893	0.0001	2841	R, Parietal Lobe, Postcentral Gyrus, BA5
	Cluster 3	−28	−86	−9	3,772	0.0002	3508	L, Occipital Lobe, Inferior Occipital Gyrus, BA18
	Cluster 4	−52	−8	12	−3,647	0.0003	4530	L, Frontal Lobe, Precentral Gyrus, BA43
Inv.Faces and scrambled HF	Cluster 1	23	−77	−9	3,931	0.00009	1611	R, Occipital Lobe, Lingual Gyrus, BA18
	Cluster 2	−1	46	15	3,396	0.0007	3059	L, Frontal Lobe, Medial Frontal Gyrus, BA9
	Cluster 3	8	−50	27	3,427	0.0006	1257	R, Limbic Lobe, Posterior Cingulate, BA23
	Cluster 4	−22	−83	−9	3,752	0.0002	7202	L, Occipital Lobe, Middle Occipital Gyrus, BA18
	Cluster 5	−25	−41	57	−3,413	0.0006	2280	L, Parietal Lobe, Sub-Gyral, BA40
	Cluster 6	−34	−44	45	−3,448	0.0006	1069	L, Parietal Lobe, Inferior Parietal Lobule, BA40
	Cluster 7	−52	−23	36	−2,688	0.0072	911	L, Parietal Lobe, Postcentral Gyrus, BA2
HF vs. LF	Cluster 1	47	−26	30	−3,434	0.0006	1077	R, Parietal Lobe, Postcentral Gyrus, BA2
	Cluster 2	−4	−59	30	3,024	0.0025	1116	L, Parietal Lobe, Precuneus, BA7
	Cluster 3	−43	1	3	−3,117	0.0018	1036	L, Sub-lobar, Insula, BA13

LF and HF stands for low frequency and high frequency respectively. R, L, and BA stands for right and left hemispheres and Broadmann Area, respectively. Clusters were obtained correcting for multiple comparisons by applying the cluster-level statistical threshold estimator from BrainVoyagerQX Plugins with 1000 iterations and alpha <0.05.

times, a main effect of condition was also present ($F = 19.502$, $P < 0.000001$). The Bonferroni post-hoc analysis revealed that subjects performed slower for the scrambled condition in comparison with all the others (mean difference: 241.09 ms, $P < 0.000001$, for scrambled vs. faces; 285.94 ms, $P < 0.000001$ for scrambled vs. guitars; 217.96 ms, $P = 0.000004$ for scrambled vs. inverted faces). On average, subjects' reaction times were 725.7 ± 88.20 ms for mooney faces, 751.20 ± 98.02 ms for upside down faces, 682.69 ± 77.81 ms for guitars and 968.22 ± 136.13 ms for scrambled conditions, well after stimulus offset (Fig. 3, right panel contains a plot summarizing these results).

Event-related Potentials

Figure 4A,B shows ERP measures for each category outside (single EEG/ERP recordings) and inside (simultaneous EEG/fMRI measurements) the scanner, respectively. After artifact correction, we were able to observe similar waveform patterns outside and inside the scanner, across conditions. We observed in both cases the expected positive P100 early visual component and a similar categorical dependent pattern around the typical face selective N170 [George et al., 2005]. Our results are in line with the report of Sadeh et al. [2008]. An one-way ANOVA with Bonferroni correction for multiple comparisons ($P < 0.05$) revealed the time points where the difference between conditions were significant (see gray bars in Fig. 4C for detailed representation of significantly different time points). Differences were found close to the N170 and latter around 300 and 400 ms. Furthermore, note that the Mooney face stimuli are evoking the largest amplitudes of the N170 (150–200 ms, $P < 0.05$).

Time–Frequency Data

We computed the time-frequency (TF) transforms of single epochs and averaged them across all trials and the posterior cluster of electrodes. In this way, we

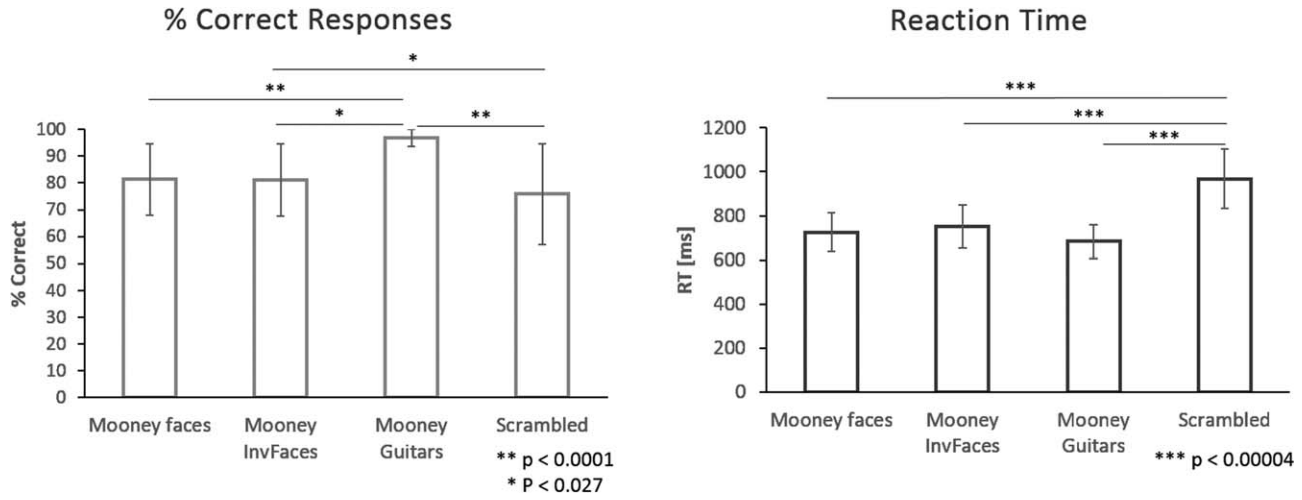

Figure 3.

Behavioral results. Left panel: bar plot showing the behavioral results per condition in terms of the discrimination rate. Significantly different comparisons are highlighted in the graph. Note that subject's best rate level is for guitars. Right panel: a bar plot representing the reaction time per condition and the statistically significant differences between them. Scrambled conditions lead to slower responses than all the other stimuli.

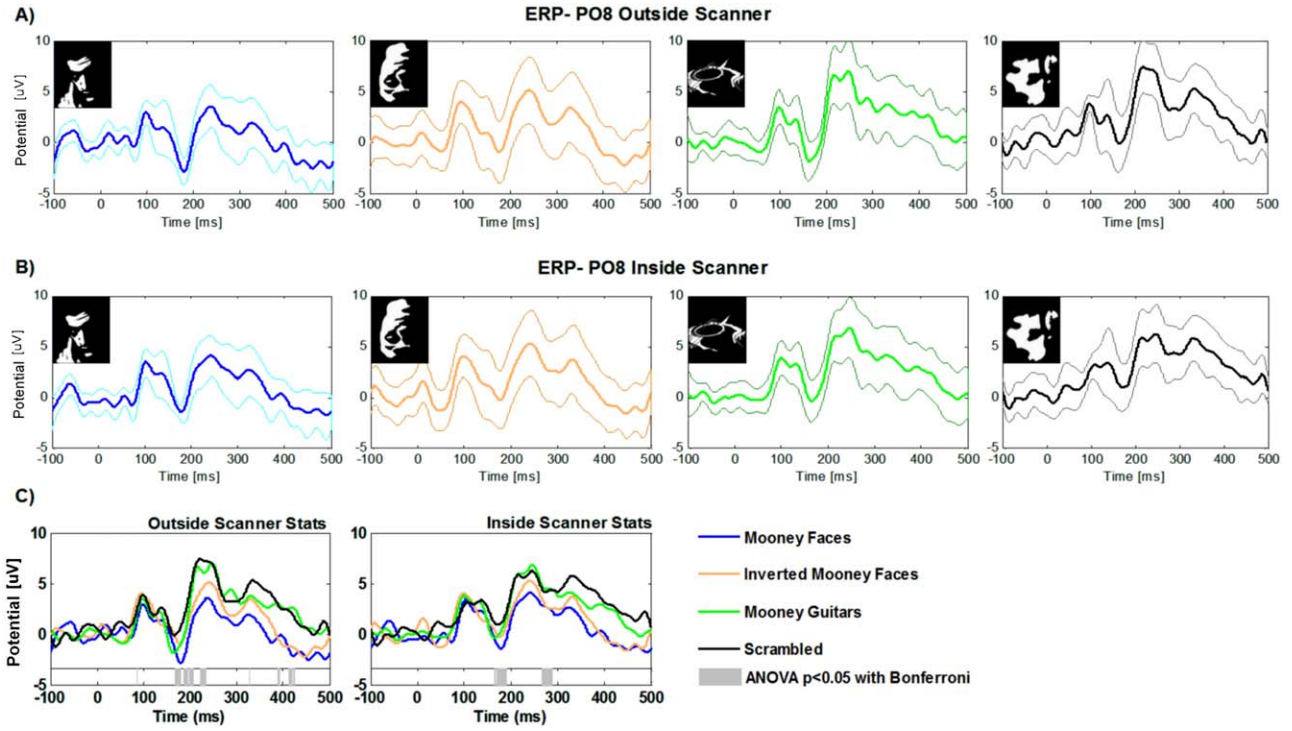

Figure 4.

Group average ERPs for EEG data acquired outside (**A**) and inside the scanner (**B**). Separate plots are shown for each condition for the PO8 electrode. Bold lines represent the group average and thicker lines the respective standard deviations. (**C**): Superimposed group average ERPs. Different colours represent ERPs for the PO8 channel for the different stimulus categories. Gray bars at the bottom show the time-points where differences are statistically significant as revealed by ANOVA with bonferroni correction ($P < 0.05$).

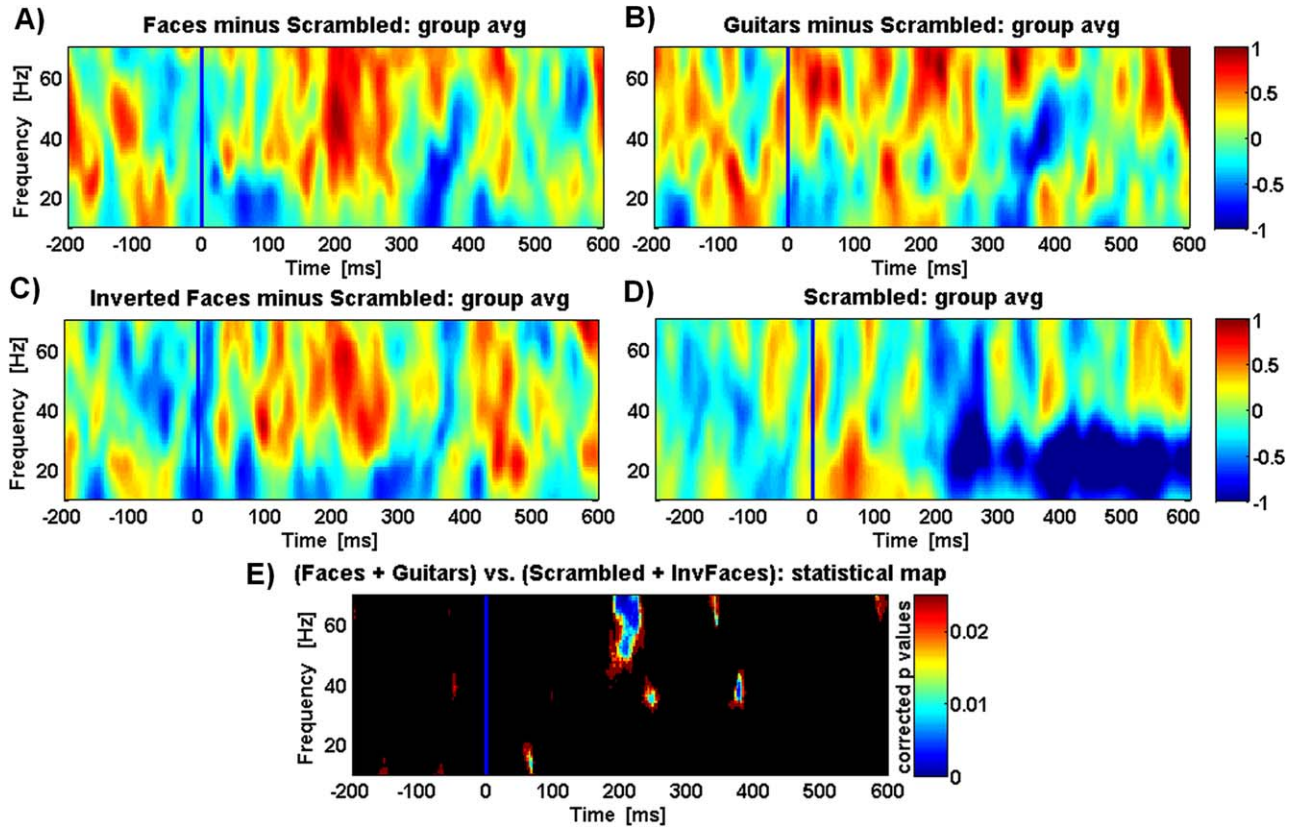

Figure 5.

Normalized time–frequency analysis reveals a similar pattern for all object categories conditions minus the scrambled (noncategorical) condition. TF results are shown for a group average of all parieto-occipital and temporal cluster of channels, for faces, guitars, and inverted faces (**A**), (**B**), and (**C**), respectively. Resulting time-frequency data from the scrambled condition (also shown in (**D**)) was subtracted in all conditions. Colour scale means normalized units (in relation to baseline pre-stimuli) and the blue line marks stimulus onset. Note that subject decision was only reported after stimulus offset (see reaction time results in Fig. 3). (**E**) plot showing the statistical p-values for the comparison between Object categories and the Scrambled conditions with the Wilcoxon–Ranksum test ($P < 0.025$). For additional information on normalized time-frequency results obtained over different clusters of channels see Figure 6.

focused on the induced gamma activity patterns which are not phase-locked to the stimulus onset. The time-frequency results are summarized in Figure 5. Time-frequency representations of gamma activity patterns for objects minus control (non-perceived) scrambled conditions are shown in Figure 5A–C for the faces, guitars and inverted faces categories respectively. We found increased activity at the gamma-band frequency range for all categories *vs*. the scrambled condition after the stimulus onset period (the TF result for the scrambled condition is shown in Fig. 5D).

The same figure shows time frequency corrected p value maps (Wilcoxon rank sum test (Matlab ®), Fig. 5E) represented in a plot showing the time-frequency points where the difference is significant ($P < 0.025$). It is noteworthy to point out that all objects *vs*. scrambled condition generate similar spectral signatures, with two bands, one at the low gamma range (~40 Hz) and the other at high gamma frequency range (~63 Hz). Moreover, scrambled conditions induced modulations dominating at lower frequency bands (high beta and low gamma) whereas object categories dominate for the higher frequency band. The time–frequency activity per electrode's cluster for both (scrambled and object) conditions is shown in Figure 6.

We found a peak (increased gamma activity) with similar average frequency of 39.44 ± 2.46 Hz and 40.28 ± 3.70 (lower gamma-band, LF) for the readily perceived objects (faces + guitars) and difficult conditions (scrambled + inverted faces), respectively. For the high gamma frequency range (HF), the peaks were found for an average frequency of 63.11 ± 3.75 Hz for objects and 62.95 ± 3.10 Hz for scrambled conditions. Mean peak amplitudes per frequency band were 9.49 ± 6.99 and

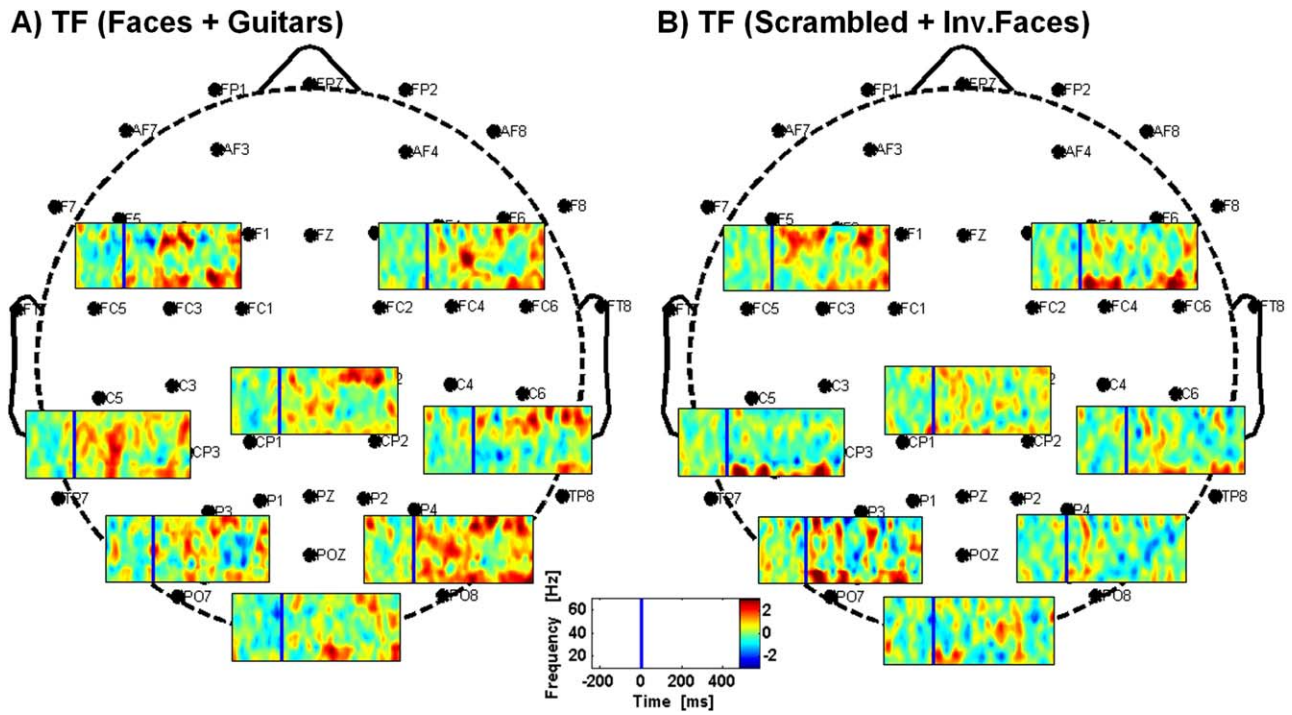

Figure 6.

Time–frequency results obtained over different clusters of channels (occipital, parietal, temporal, frontal, and those left and right). (**A**) Time–frequency results for the faces + guitars condition; (**B**) Time-frequency results for the scrambled + inverted faces condition. Colorscale means normalized units (data normalized for the time preceding stimuli presentation) and the blue line marks the stimuli onset.

7.97 ± 3.78 (power) for objects and scrambled LF respectively, and 14.09 ± 3.13 for objects HF and 7.75 ± 3.72 for scrambled HF. Differences between peak frequencies of objects vs. scrambled were not significant neither for frequencies ($t = -0.71$, $P = 0.5$ for LF; $t = 0.10$, $P = 0.920$ for HF) nor for amplitudes ($t = 1.009$, $P = 0.347$ for LF and $t = 1.228$, $P = 0.259$ for HF). Moreover, no correlation was found between differences in amplitude and differences in reaction times (RT; Pearson = 0.017, $P = 0.967$ for LF and Pearson correlation = 0.294, $P = 0.479$ for HF) or between differences in discrimination rates and differences in peak amplitudes (Pearson = 0.5, $P = 0.253$).

Source Localization Based on the EEG Data

We performed source localization of group average ERPs using Curry 7.0 (NeuroScan, USA) for each stimulus category and found the expected ERP sources of activity at visual ventral regions 170 ms after stimulus onset. All object perception conditions showed indeed similar bilateral infero-temporal activations (Fig. 7A–C) that are distinct from the one evoked by the scrambled control (no object perception) condition (see Fig. 7D). Right hemisphere dominates for the faces, inverted faces and scrambled conditions while left temporal regions appear for the guitars. We only found dominant occipital and frontal regions for the scrambled (absent visual category) condition. Results shown in Figure 7 are displayed for the hemisphere revealing activity over a threshold of 75% of the CSD (see figure legend for *F*-distribution values per condition).

In addition, we performed time–frequency decomposition using Curry 7.0 software and calculated the current source density maps as revealed by sLORETA. We separated the analysis by conditions and low and high frequency ranges. Figure 8 summarizes the results for these frequency bands. The activity for the low frequency (LF) band (Fig. 8A–D) emerges mainly at infero-frontal regions (insula plus frontal operculum) known to be related to decision processes. This pattern is similar for all stimulus conditions. On the other hand, high frequency patterns (HF; Fig. 8E–H) show distributed activity sources that differ depending on the condition. The faces are localized to parietal regions, inverted faces sources are localized to right temporal regions, while guitars show a pattern with conspicuously localized sources at frontal areas. In contrast, the scrambled (non-recognizable object) condition shows a different pattern reminiscent to the one observed with ERP source localization with dominant occipital and frontal regions.

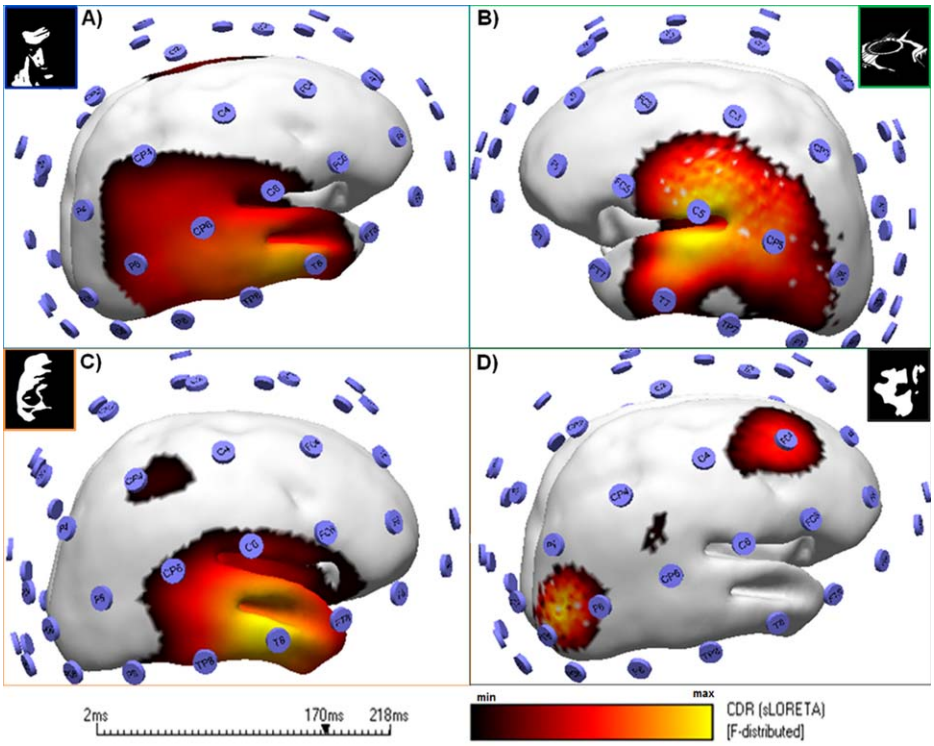

Figure 7.

Categorical perception leads to a pattern that is distinct from perception of random (scrambled) patterns. Source localization of group average ERPs reveals sources of activity at visual ventral regions. Results are shown for the N170 latency point. Colour codes correspond to the range of min and max CDR distribution values based in sLORETA. Right hemisphere dominates for the faces (*F*-distributed (min–max): 5.2–6.7), inverted faces (*F*-distributed 3.9–5.6) and scrambled condition (*F*-distributed 5.0–7.0) while left temporal regions appear for the guitars (*F*-distributed 3.3–4.2). Note that all object conditions (**A–C**) have a similar infero-temporal pattern that differed from the one evoked by scrambled conditions (**D**). A display threshold of 75% of the CSD was applied and the sources are shown for the hemisphere that revealed higher activity. [Color figure can be viewed in the online issue, which is available at wileyonlinelibrary.com.]

Source Localization With EEG Informed fMRI Approach

Using a general linear model analysis of the fMRI data, to model the neural origins of the different gamma activity patterns, we were able to identify two different neural generators for these distinct frequency bands. To precisely localize these patterns of gamma-band activity we used the latencies (on a trial by trial basis, per subject) of the gamma activity peaks as event predictors of a GLM modeling the EEG oscillations. Separate predictors for the low (30–48 Hz) and high (52–70 Hz) frequencies were constructed [Scheeringa et al., 2011]. Differences in latency peaks between conditions were not significant (LF, object vs. scrambled: $F = 0.231$, $P = 0.634$; HF, object vs. scrambled: $F = 0.075$, $P = 0.786$). Results show that posterior sources mainly located at the parieto-occipital and temporal lobes were strongly linked to the higher gamma frequency band but also for the LF band, in particular for object category perception (Fig. 9A,C).

We found that different gamma sources are related to perception processes in decision related regions centered in the anterior insula (Fig. 9B,E) and in the visual processing areas (Fig. 9C,D); see also Supporting Information Figure 1 with stimulus locked fMRI localization). Low gamma frequency related activity in the anterior insula was particularly strong, which is interesting given the role of this region in perceptual decision [Rebola et al., 2012] (Fig. 9B; see Table I for details regarding regions' coordinates, cluster sizes and statistics). Furthermore, a dissociation was visible for the LF sources between perceived objects and scrambled conditions. Interestingly, activity for object percepts was lateralized to the right insula while for scrambled conditions it was higher at the left anterior insula. Negative BOLD activity, as measured by EEG-informed fMRI was visible for different contrasts. These activations were found to the scrambled LF predictors localized in areas spanning from occipital regions to anterior areas including the sub-lobular insula and the anterior cingulate. Regarding the HF predictors, negative activity

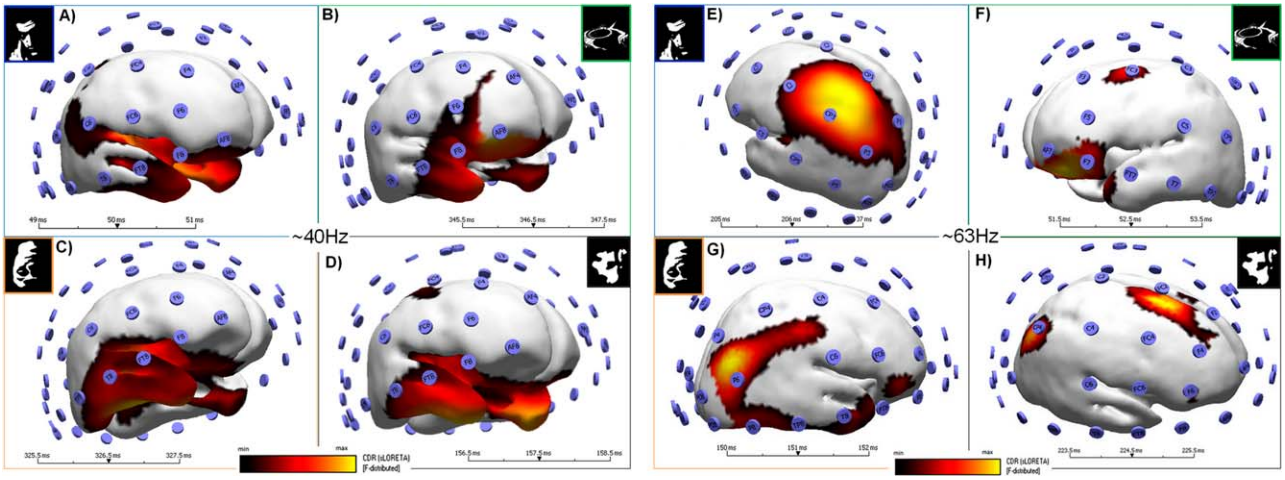

Figure 8.

Source localization of gamma activity patterns reveals distinct sources for LF and HF bands. (**A–D**) show current source density maps per condition for the LF gamma activity band. (**E–H**) are the source maps per condition for the HF band. Colorscale corresponds to the range of min and max values of source maps. Sources were present in both hemispheres (a display threshold of 75% of the CSD was applied). The faces are localized to parietal regions (*F*-distributed min–max varied between 11.0–14.7 and 3.8–5.0 for LF and HF, respectively), inverted faces sources are localized to right temporal regions (*F*-distributed: 2.0–2.7 for LF and 16.0–22.0 for HF) while guitars show sources at frontal areas (*F*-distributed: 6.7–8.8 for LF and 4.1–5.9 for HF). In contrast, the scrambled (non-recognizable object) condition source localization have dominant occipital and frontal regions (*F*-distributed: 6.6–8.7 for LF and 3.0–5.1 for HF). [Color figure can be viewed in the online issue, which is available at wileyonlinelibrary.com.]

was found for parietal and frontal regions (see Table I for details). Figure 9E,F show the GLM results for the two direct contrasts: HF higher than LF and *vice versa*, respectively. Note that posterior (visual) activation is evident for the HF > LF and bilateral anterior activation on the insula/operculum is present for the LF > HF contrast.

DISCUSSION

In this simultaneous EEG/fMRI study we found that different gamma oscillatory patterns corresponding to different brain regions/networks can be separated within the same perceptual decision-making task. These regions were identified as visual and insular networks. High gamma band patterning (~60 Hz) dominated in visual regions and a lower band (~40 Hz) dominated in the anterior insula, which is a region known to be involved in high level decision processes [Heekeren et al., 2008]. Both visual and insular sources are known to be important for perceptual decision making and gestalt formation [Grützner et al., 2010; Rebola et al., 2012]. We observed that under difficult decision conditions, when an object category was harder to detect, the insula showed a higher modulation. This is precisely the region most closely associated with higher beta and low gamma frequency modulation (together with the anterior cingulate [Lee et al., 2007], which is involved in conflict monitoring [Botvinick et al., 2004]). Larger activity modulation at the higher frequency gamma-band around decision time was present for holistic categorical (object) vs. noncategorical (scrambled) perception. Such a dissection of the cognitive and neural components of perceptual decision suggests that different gamma sub-bands can be related to separable circuits within the same cognitive task.

Different Gamma sub-bands had been previously identified in different cortical regions and tasks [Akimoto et al., 2013; Crone et al., 2011; Edwards et al., 2005; Fries et al., 2008; Groppe et al., 2013; Gruber et al., 2008; Grützner et al., 2010; Hoogenboom et al., 2006; Jerbi et al., 2009; Koelewijn et al., 2013; Lachaux et al., 2005; Ray and Maunsell, 2011; Sedley and Cunningham, 2013; Uchida et al., 2001] but the focus of this study was whether distinct patterns could be found within the same task.

Current source density approaches in the above mentioned studies had found evidence for gamma patterns characterized by different frequencies, for different tasks. However, these did not have enough resolution (as here provided by combination of EEG and fMRI) to test for non-unitary sources and establish their spatial topography within the same task.

Separability of different sources of gamma activity [Koelewijn et al., 2013] had been suggested to occur within the same visual region (lateral and medial visual cortex). Koelewijn et al. have indeed found that a rotating grating induced gamma synchronization in medial visual cortex at

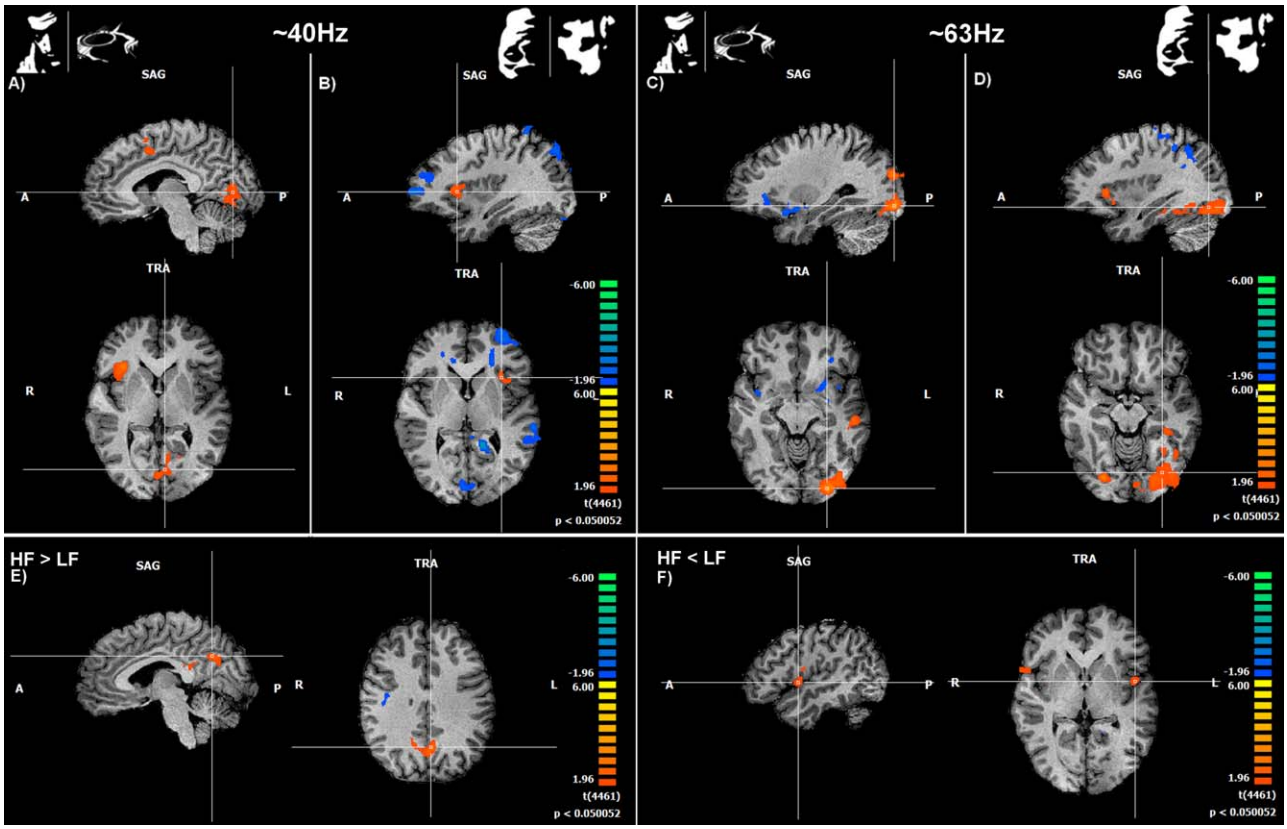

Figure 9.

EEG-informed fMRI evidence for different neural generators for distinct frequency bands, one related to visual processing (early visual areas) and the other to high level decision mechanisms (e.g., the insula). (**A**) and (**B**) show GLM maps based on gamma-band regressors—low frequency (LF) for face + guitar objects (easily perceived) and inverted faces + scrambled conditions (not readily perceived), respectively. High frequency (HF) GLM maps are shown in (**C**) and (**D**). Note that group analyses showed different significantly activated regions as a function of frequency band. We found increased activity for decision related areas (anterior insula) mainly for the LF predictor (low gamma range; A) and B)). Visual areas activated in particular in response to higher Gamma oscillation predictors which are related to object perception (C) and scrambled conditions (D). (**E**): brain regions activated for the contrast HF > LF. (**F**): areas with increased modulation for the LF > HF contrast. Map threshold was set to $P < 0.05$ (corrected). See Table I for details regarding significant clusters sizes, and locations and statistics.

30–70 Hz, and in lateral visual cortex at 60–90 Hz. Directing spatial attention to the grating increased gamma synchronization in medial visual cortex, but only at 60–90 Hz [Koelewijn et al., 2013], which is in the range identified in our study for visual regions.

These results are also consistent with MEG study of Gruber et al. [2008] on gamma-band generators in focal visual areas. We argue that these generators reflect local processing [Schnitzler and Gross, 2005].

Our previous EEG study in Williams syndrome [Bernardino et al., 2013] suggested that sub-bands related to either visual or high level processing can be differentially modulated as a function of the cognitive strategy, suggesting the recruitment of multiple cognitive modules, and also inspired the current study.

Following those findings we found that predictors for increased activity at higher gamma-band have their origin in low-level visual areas in particular during object perception, during which top-down perceptual effects dominate. On the other hand, predictors for the low frequency range have their source at anterior decision related areas, namely the insula. In spite of the fact that the dissociation between two frequency bands within the same experiment has already been reported from auditory cortex recordings [Edwards et al., 2005], the duality we found and its relation to distinct cognitive mechanisms within the same task was not identified before. These gamma sub-bands show different frequencies, different brain generators and different functional meaning, one related to visual processing and the other to perceptual

decision-making. This was rendered possible by our simultaneous EEG/fMRI [Logothetis, 2008] and the EEG source localization approaches which enabled to pinpoint the above described unexpected dichotomy of gamma activity during perceptual decision. EEG/fMRI yields better localization resolution than MEG, which has nevertheless been shown to have considerably better accuracy in localization than EEG.

Gamma oscillations are known to be stimulus-induced [Hoogenboom et al., 2006; Muthukumaraswamy et al., 2010] and are closely colocalized to the blood-oxygen-level-dependent (BOLD) response [Koch et al., 2009; Logothetis et al., 2001]. Our finding that a clear functional and topographic distinction is present for separable anatomo-physiological substrates of gamma sub-bands may shed light on the controversy between studies that reported the differential patterns of correlation between BOLD and gamma-band oscillations [Foucher et al., 2003; Logothetis et al., 2001; Michels et al., 2010; Muthukumaraswamy and Singh, 2008, 2009; Scheeringa et al., 2011; Sumiyoshi et al., 2012]. Therefore our results provide support to the idea that low- and high-frequency oscillations reflect different phenomena and may be caused by different mechanisms [Guggisberg et al., 2007; Logothetis et al., 2001; Ray and Maunsell, 2011; Scheeringa et al., 2011] within the same task. Although we were limited by the artifact correction algorithms that restrict the frequency range one can analyze (maximum ~70 Hz), our results do indeed support the notion that gamma-band activity patterns (low and high gamma sub-bands) are not related to holistic perception in a simple unified manner, since aspects related to visual processing and decision can clearly be separated in terms of their neural origins. Based on the information provided by time-frequency EEG analysis, we were able to determine their spatio-temporal profile.

An analogous distinction between sub-bands was also discussed recently in a review by Sedley and Cunnigham differentiating gamma activity in terms of narrow versus broad-band patterns [Sedley and Cunningham, 2013], with putatively distinct physiological meaning. Accordingly, Ray and Maunsell showed that in monkey multi-unit recordings, higher frequency oscillations only were associated with spiking rate, which was not the case for lower gamma oscillations [Ray and Maunsell, 2011]. Interestingly the lower frequency oscillations that we observed were mostly related to the insula and not the visual cortex.

Concerning the negative BOLD response which is also known to reflect stimulus related and/or neurophysiological responses [Duarte et al., 2013; Marques et al., 2009; Shmuel et al., 2002, 2006; Smith et al., 2004] we also identified a network that deactivated mainly in response to scrambled object conditions, in particular in anterior regions.

In sum, we could identify spatial substrates underlying the temporal dynamics of brain activity [Herrmann and Debener, 2008; Laufs, 2008; Ritter and Villringer, 2006] during perceptual decision and categorization. Our results indicate the existence of distinct low and high level functional modules in the same perceptual decision task that can be tagged by two distinct frequency bands. These findings are relevant for the understanding of normal and clinical impaired holistic integration and show that current neuronal models of gamma-band spatial distribution need to consider their duality by separating low and high sub-bands.

CONCLUSIONS

We conclude that gamma-band activity patterns do not represent a unitary phenomenon within the same decision task, but rather distinct neurocognitive components. Accordingly, at least two separate neural modules are involved in holistic perceptual decision, one in the visual cortex and the other in the anterior insula. This provides a step forward in understanding the functional specialization of decision-making networks and the role of gamma frequency range sub-bands in signaling their different neural and cognitive components. The finding that gestalt formation elicits non unitary gamma-band patterns, underlying independent sensory processing and perceptual decision mechanisms is novel and may shed new light on the role of gamma-band response in normal cognition and in neuropsychiatric disorders such as autism and schizophrenia, where both visual and decision making circuits may be impaired [Uhlhaas and Singer, 2012]. Further studies including electrocorticography and non-simultaneous MEG and fMRI studies may help elucidating their separability with even higher spatial resolution.

ACKNOWLEDGEMENTS

The authors thank the anonymous reviewers for helping improving the manuscript.

REFERENCES

Akimoto Y, Kanno A, Kambara T, Nozawa T, Sugiura M, Okumura E, Kawashima R (2013): Spatiotemporal dynamics of high-gamma activities during a 3-stimulus visual oddball task. PLoS One 8:e59969.

Allen PJ, Polizzi G, Krakow K, Fish DR, Lemieux L (1998): Identification of EEG events in the MR scanner: The problem of pulse artifact and a method for its subtraction. Neuroimage 8: 229–239.

Allen PJ, Josephs O, Turner R (2000): A method for removing imaging artifact from continuous EEG recorded during functional MRI. Neuroimage 12:230–239.

Bernardino I, Castelhano J, Farivar R, Silva ED, Castelo-Branco M (2013): Neural correlates of visual integration in Williams syndrome: Gamma oscillation patterns in a model of impaired coherence. Neuropsychologia 51:1287–1295.

Botvinick MM, Cohen JD, Carter CS (2004): Conflict monitoring and anterior cingulate cortex: An update. Trends Cogn Sci 8: 539–546.

Brookes MJ, Vrba J, Mullinger KJ, Geirsdóttir GB, Yan WX, Stevenson CM, Bowtell R, Morris PG (2009): Source localisation in concurrent EEG/fMRI: Applications at 7T. Neuroimage 45:440–452.

Castelhano J, Rebola J, Leitão B, Rodriguez E, Castelo-Branco M (2013): To perceive or not perceive: The role of gamma-band activity in signaling object percepts, Ward LM, editor. PLoS One 8:e66363.

Castelo-Branco M, Neuenschwander S, Singer W (1998): Synchronization of visual responses between the cortex, lateral geniculate nucleus, and retina in the anesthetized cat. J Neurosci 18: 6395–6410.

Crone NE, Korzeniewska A, Franaszczuk PJ (2011): Cortical γ responses: Searching high and low. Int J Psychophysiol 79:9–15.

De Munck JC, van Houdt PJ, Gonçalves SI, van Wegen E, Ossenblok PPW (2013): Novel artefact removal algorithms for co-registered EEG/fMRI based on selective averaging and subtraction. Neuroimage 64:407–415.

Debener S, Ullsperger M, Siegel M, Engel AK (2006): Single-trial EEG-fMRI reveals the dynamics of cognitive function. Trends Cogn Sci 10:558–563.

Debener S, Mullinger KJ, Niazy RK, Bowtell RW (2008): Properties of the ballistocardiogram artefact as revealed by EEG recordings at 1.5, 3 and 7 T static magnetic field strength. Int J Psychophysiol 67:189–199.

Delorme A, Makeig S (2004): EEGLAB: An open source toolbox for analysis of single-trial EEG dynamics including independent component analysis. J Neurosci Methods 134:9–21.

Duarte IC, Cunha G, Castelhano J, Sales F, Reis A, Cunha JPS, Castelo-Branco M (2013): Developmental dissociation of visual dorsal stream parvo and magnocellular representations and the functional impact of negative retinotopic BOLD responses. Brain Cogn 83:72–79.

Edwards E, Soltani M, Deouell LYLY, Berger MSMS, Knight RTRT (2005): High gamma activity in response to deviant auditory stimuli recorded directly from human cortex. J Neurophysiol 94:4269.

Ertl M, Kirsch V, Leicht G, Karch S, Olbrich S, Reiser M, Hegerl U, Pogarell O, Mulert C (2010): Avoiding the ballistocardiogram (BCG) artifact of EEG data acquired simultaneously with fMRI by pulse-triggered presentation of stimuli. J Neurosci Methods 186:231–241.

Foucher JR, Otzenberger H, Gounot D (2003): The BOLD response and the gamma oscillations respond differently than evoked potentials: An interleaved EEG-fMRI study. BMC Neurosci 4: 22.

Freyer F, Becker R, Anami K, Curio G, Villringer A, Ritter P (2009): Ultrahigh-frequency EEG during fMRI: Pushing the limits of imaging-artifact correction. Neuroimage 48:94–108.

Fries P (2009): Neuronal gamma-band synchronization as a fundamental process in cortical computation. Annu Rev Neurosci 32:209–224.

Fries P, Scheeringa R, Oostenveld R (2008): Finding gamma. Neuron 58:303–305.

George N, Jemel B, Fiori N, Chaby L, Renault B (2005): Electrophysiological correlates of facial decision: Insights from upright and upside-down Mooney-face perception. Brain Res Cogn Brain Res 24:663–673.

Gonçalves SI, Pouwels PJW, Kuijer JPA, Heethaar RM, de Munck JC (2007): Artifact removal in co-registered EEG/fMRI by selective average subtraction. Clin Neurophysiol 118:2437–2450.

Groppe DM, Bickel S, Keller CJ, Jain SK, Hwang ST, Harden C, Mehta AD (2013): Dominant frequencies of resting human brain activity as measured by the electrocorticogram. Neuroimage 79:223–233.

Gruber T, Keil A, Müller MM (2001): Modulation of induced gamma band responses and phase synchrony in a paired associate learning task in the human EEG. Neurosci Lett 316:29–32.

Gruber T, Maess B, Trujillo-Barreto NJJ, Müller MM (2008): Sources of synchronized induced gamma-band responses during a simple object recognition task: A replication study in human MEG. Brain Res 1196:74–84.

Grützner C, Uhlhaas PJ, Genc E, Kohler A, Singer W, Wibral M (2010): Neuroelectromagnetic correlates of perceptual closure processes. J Neurosci 30:8342–8352.

Guggisberg AG, Dalal SS, Findlay AM, Nagarajan SS (2007): High-frequency oscillations in distributed neural networks reveal the dynamics of human decision making. Front Hum Neurosci 1:14.

Heekeren HR, Marrett S, Ungerleider LG (2008): The neural systems that mediate human perceptual decision making. Nat Rev Neurosci 9:467–479.

Herrmann CS, Debener S (2008): Simultaneous recording of EEG and BOLD responses: A historical perspective. Int J Psychophysiol 67:161–168.

Hoogenboom N, Schoffelen J-M, Oostenveld R, Parkes LM, Fries P (2006): Localizing human visual gamma-band activity in frequency, time and space. Neuroimage 29:764–773.

Huster RJ, Debener S, Eichele T, Herrmann CS (2012): Methods for simultaneous EEG-fMRI: An introductory review. J Neurosci 32:6053–6060.

Jensen O, Kaiser J, Lachaux J-P (2007): Human gamma-frequency oscillations associated with attention and memory. Trends Neurosci 30:317–324.

Jerbi K, Ossandón T, Hamamé CMCM, Senova S, Dalal SSSS, Jung J, Minotti L, Bertrand O, Berthoz A, Kahane P, Lachaux J-P (2009): Task-related gamma-band dynamics from an intracerebral perspective: Review and implications for surface EEG and MEG. Hum Brain Mapp 30:1758–1771.

Keil A, Müller MM, Ray WJ, Gruber T, Elbert T (1999): Human gamma band activity and perception of a gestalt. J Neurosci 19:7152–7161.

Keren AS, Yuval-Greenberg S, Deouell LY (2010): Saccadic spike potentials in gamma-band EEG: Characterization, detection and suppression. Neuroimage 49:2248–2263.

Koch SP, Werner P, Steinbrink J, Fries P, Obrig H (2009): Stimulus-induced and state-dependent sustained gamma activity is tightly coupled to the hemodynamic response in humans. J Neurosci 29:13962–13970.

Koelewijn L, Rich AN, Muthukumaraswamy SD, Singh KD (2013): Spatial attention increases high-frequency gamma synchronisation in human medial visual cortex. Neuroimage 79:295–303.

Lachaux J-P, Rodriguez E, Martinerie J, Varela FJ (1999): Measuring phase synchrony in brain signals. Hum Brain Mapp 8: 194–208.

Lachaux J-P, George N, Tallon-Baudry C, Martinerie J, Hugueville L, Minotti L, Kahane P, Renault B (2005): The many faces of the gamma band response to complex visual stimuli. Neuroimage 25:491–501.

Lachaux J-P, Fonlupt P, Kahane P (2007): Relationship between task-related gamma oscillations and BOLD signal: New insights from combined fMRI and intracranial EEG. Hum Brain Mapp 28:1368–1375.

Laufs H (2008): Endogenous brain oscillations and related networks detected by surface EEG-combined fMRI. Hum Brain Mapp 29:762–769.

Lee B, Park KS, Kang D-H, Kang KW, Kim YY, Kwon JS (2007): Generators of the gamma-band activities in response to rare and novel stimuli during the auditory oddball paradigm. Neurosci Lett 413:210–215.

Logothetis NK (2008): What we can do and what we cannot do with fMRI. Nature 453:869–878.

Logothetis NK, Pauls J, Augath M, Trinath T, Oeltermann A (2001): Neurophysiological investigation of the basis of the fMRI signal. Nature 412:150–157.

Mandelkow H, Halder P, Boesiger P, Brandeis D (2006): Synchronization facilitates removal of MRI artefacts from concurrent EEG recordings and increases usable bandwidth. Neuroimage 32:1120–1126.

Mantini D, Perrucci MG, Cugini S, Ferretti A, Romani GL, Del Gratta C (2007a): Complete artifact removal for EEG recorded during continuous fMRI using independent component analysis. Neuroimage 34:598–607.

Mantini D, Perrucci MG, Del Gratta C, Romani GL, Corbetta M (2007b): Electrophysiological signatures of resting state networks in the human brain. Proc Natl Acad Sci USA 104:13170–13175.

Marques JP, Rebola J, Figueiredo P, Pinto A, Sales F, Castelo-Branco M (2009): ICA decomposition of EEG signal for fMRI processing in epilepsy. Hum Brain Mapp 30:2986–2996.

Martinovic J, Gruber T, Hantsch A, Müller MM (2008): Induced gamma-band activity is related to the time point of object identification. Brain Res 1198:93–106.

Michels L, Bucher K, Lüchinger R, Klaver P, Martin E, Jeanmonod D, Brandeis D (2010): Simultaneous EEG-fMRI during a working memory task: Modulations in low and high frequency bands. PLoS One 5:e10298.

Mooney CM (1957): Age in the development of closure ability in children. Can J Psychol 11:219–226.

Muthukumaraswamy SD, Singh KD (2008): Spatiotemporal frequency tuning of BOLD and gamma band MEG responses compared in primary visual cortex. Neuroimage 40:1552–1560.

Muthukumaraswamy SD, Singh KD (2009): Functional decoupling of BOLD and gamma-band amplitudes in human primary visual cortex. Hum Brain Mapp 30:2000–2007.

Muthukumaraswamy SD, Singh KD, Swettenham JB, Jones DK (2010): Visual gamma oscillations and evoked responses: Variability, repeatability and structural MRI correlates. Neuroimage 49:3349–3357.

Nguyen VT, & Cunnington R (2014): The superior temporal sulcus and the N170 during face processing: single trial analysis of concurrent EEG-fMRI. NeuroImage 86:492–502.

Niessing J, Ebisch B, Schmidt K (2005): Hemodynamic signals correlate tightly with synchronized gamma oscillations. Science 80:948.

Pascual-Marqui R (1999): Review of methods for solving the EEG inverse problem. Int J Bioelectromagn 1:75–86.

Pascual-Marqui R (2002): Standardized low-resolution brain electromagnetic tomography (sLORETA): Technical details. Methods Find Exp Clin Pharmacol 24:5–12.

Pascual-Marqui RD, Michel CM, Lehmann D (1994): Low resolution electromagnetic tomography: A new method for localizing electrical activity in the brain. Int J Psychophysiol 18:49–65.

Pascual-Marqui RD, Esslen M, Kochi K, Lehmann D (2002): Functional imaging with low-resolution brain electromagnetic tomography (LORETA): A review. Methods Find Exp Clin Pharmacol 24 (Suppl C):91–95.

Ray S, Maunsell JHR (2011): Different origins of gamma rhythm and high-gamma activity in macaque visual cortex. PLoS Biol 9:e1000610.

Rebola J, Castelhano J, Ferreira C, Castelo-Branco M (2012): Functional parcellation of the operculo-insular cortex in perceptual decision making: An fMRI study. Neuropsychologia 50:3693–3701.

Ritter P, Villringer A (2006): Simultaneous EEG-fMRI. Neurosci Biobehav Rev 30:823–838.

Rodriguez E, George N, Lachaux JP, Martinerie J, Renault B, Varela FJ (1999): Perception's shadow: Long-distance synchronization of human brain activity. Nature 397:430–433.

Rosenkranz K, Lemieux L (2010): Present and future of simultaneous EEG-fMRI. MAGMA 23:309–316.

Sadeh B, Zhdanov A, Podlipsky I, Hendler T, Yovel G (2008): The validity of the face-selective ERP N170 component during simultaneous recording with functional MRI. Neuroimage 42: 778–786.

Scheeringa R, Petersson KM, Oostenveld R, Norris DG, Hagoort P, Bastiaansen MCM (2009): Trial-by-trial coupling between EEG and BOLD identifies networks related to alpha and theta EEG power increases during working memory maintenance. Neuroimage 44:1224–1238.

Scheeringa R, Fries P, Petersson K-M, Oostenveld R, Grothe I, Norris DG, Hagoort P, Bastiaansen MCM (2011): Neuronal dynamics underlying high- and low-frequency EEG oscillations contribute independently to the human BOLD signal. Neuron 69:572–583.

Sedley W, Cunningham MO (2013): Do cortical gamma oscillations promote or suppress perception? An under-asked question with an over-assumed answer. Front Hum Neurosci 7:595.

Shmuel A, Yacoub E, Pfeuffer J, Van de Moortele PF, Adriany G, Hu X, Ugurbil K (2002): Sustained negative BOLD, blood flow and oxygen consumption response and its coupling to the positive response in the human brain. Neuron 36:1195–1210.

Shmuel A, Augath M, Oeltermann A, Logothetis NK (2006): Negative functional MRI response correlates with decreases in neuronal activity in monkey visual area V1. Nat Neurosci 9:569–577.

Smith AT, Williams AL, Singh KD (2004): Negative BOLD in the visual cortex: Evidence against blood stealing. Hum Brain Mapp 21:213–220.

Sumiyoshi A, Suzuki H, Ogawa T, Riera JJ, Shimokawa H, Kawashima R (2012): Coupling between gamma oscillation and fMRI signal in the rat somatosensory cortex: Its dependence on systemic physiological parameters. Neuroimage 60: 738–746.

Tallon-Baudry C, Bertrand O (1999): Oscillatory gamma activity in humans and its role in object representation. Trends Cogn Sci 3:151–162.

Uchida S, Maehara T, Hirai N, Okubo Y, Shimizu H (2001): Cortical oscillations in human medial temporal lobe during wakefulness and all-night sleep. Brain Res 891:7–19.

Uhlhaas PJJ, Singer W (2012): Neuronal dynamics and neuropsychiatric disorders: Toward a translational paradigm for dysfunctional large-scale networks. Neuron 75:963–980.

Uhlhaas PJ, Linden DEJ, Singer W, Haenschel C, Lindner M, Maurer K, Rodriguez E (2006): Dysfunctional long-range coordination of neural activity during Gestalt perception in schizophrenia. J Neurosci 26:8168–8175.

Uhlhaas PJ, Pipa G, Neuenschwander S, Wibral M, Singer W (2011): A new look at gamma? High- (>60 Hz) γ-band activity in cortical networks: Function, mechanisms and impairment. Prog Biophys Mol Biol 105:14–28.

Varela F, Lachaux J, Rodriguez E, Martinerie J (2001): The brainweb: Phase large-scale integration. Nat Rev Neurosci 2: 229–239.